SEAGLE – I. A pipeline for simulating and modelling strong lenses from cosmological hydrodynamic simulations

Sampath Mukherjee,[1]* Léon V. E. Koopmans,[1] R. Benton Metcalf,[2,3] Nicolas Tessore,[4] Crescenzo Tortora,[1] Matthieu Schaller,[5] Joop Schaye,[5] Robert A. Crain,[6] Georgios Vernardos,[1] Fabio Bellagamba[2,3] and Tom Theuns[7]

[1]*Kapteyn Astronomical Institute, University of Groningen, PO Box 800, NL-9700 AV Groningen, the Netherlands*
[2]*Dipartimento di Fisica e Astronomia, Università di Bologna, via Gobetti 93/2, I-40129 Bologna, Italy*
[3]*Istituto Nazionale di Astrofisica (INAF) – Osservatorio di Astrofisica e Scienza dello Spazio di Bologna, via Gobetti 93/3, I-40129 Bologna, Italy*
[4]*Jodrell Bank Centre for Astrophysics, University of Manchester, Alan Turing Building, Manchester M13 9PL, UK*
[5]*Leiden Observatory, Leiden University, PO Box 9513, NL-2300 RA Leiden, the Netherlands*
[6]*Astrophysics Research Institute, Liverpool John Moores University, 146 Brownlow Hill, Liverpool L3 5RF, UK*
[7]*Institute for Computational Cosmology, Department of Physics, University of Durham, South Road, Durham DH1 3LE, UK*

ABSTRACT

In this paper we introduce the *SEAGLE* (i.e. Simulating EAGLE LEnses) programme, which approaches the study of galaxy formation through strong gravitational lensing, using a suite of high-resolution hydrodynamic simulations, Evolution and Assembly of GaLaxies and their Environments (EAGLE) project. We introduce the simulation and analysis pipeline and present the first set of results from our analysis of early-type galaxies. We identify and extract an ensemble of simulated lens galaxies and use the GLAMER ray-tracing lensing code to create mock lenses similar to those observed in the Sloan Lens ACS Survey (SLACS) and SL2S surveys, using a range of source parameters and galaxy orientations, including observational effects such as the point spread function, pixelization, and noise levels, representative of single-orbit observations with the *Hubble Space Telescope* (*HST*) using the ACS-*F*814*W* filter. We subsequently model these mock lenses using the code LENSED, treating them in the same way as observed lenses. We also estimate the mass model parameters directly from the projected surface mass density of the simulated galaxy, using an identical mass model family. We perform a three-way comparison of all the measured quantities with real lenses. We find the average total density slope of EAGLE lenses, $t = 2.26$ (0.25 rms) to be higher than SL2S, $t = 2.16$ or SLACS, $t = 2.08$. We find a very strong correlation between the external shear (γ) and the complex ellipticity (ϵ), with $\gamma \sim \epsilon/4$. This correlation indicates a degeneracy in the lens mass modelling. We also see a dispersion between lens modelling and direct fitting results, indicating systematical biases.

Key words: gravitational lensing: strong – methods: numerical – galaxies: evolution – galaxies: formation.

1 INTRODUCTION

Massive early-type galaxies (ETGs) are expected to form during the later stages in the hierarchical formation process (Blumenthal et al. 1984; Frenk et al. 1985). ETGs in the local Universe follow a number of well-known relations or correlations between their velocity dispersion, stellar age, chemical composition (Bender, Burstein &

Faber 1992, 1993), and exhibit a small scatter around the nearly-isothermal central density profiles (e.g. Rusin et al. 2003a; Rusin, Kochanek & Keeton 2003b; Rusin & Kochanek 2005; Koopmans et al. 2006, 2009). Galaxy formation models are only now beginning to address the origin of these empirical scaling relations accounting for the physical processes that play a role in their formation. There are various possibilities for their formation, for example via monolithic collapse (Eggen 1965; Searle & Zinn 1978), mergers of lower mass (disc) galaxies (Toomre & Toomre 1972; Schweizer 1982), satellite accretion (Searle & Zinn 1978), and hierarchical

* E-mail: sampath@astro.rug.nl

merging (White & Rees 1978; Fall 1983). Various environmentally dependent evolutionary processes such as stripping (Gunn & Gott 1972), cannibalism (Ostriker & Hausman 1977), stretching (Barnes & Hernquist 1992), harassment (Moore et al. 1998), strangulation (Balogh & Morris 2000), squelching (Tully et al. 2002), and splash-back (Fukugita & Peebles 2006) have been proposed to explain the formation-mechanisms of ETGs. The explicit study of their structure (Navarro, Frenk & White 1996; Moore et al. 1998), formation, and subsequent evolution provides a powerful test of the (dis)agreement between observations and the Lambda cold dark matter (ΛCDM) paradigm.

Loeb & Peebles (2003) suggest that the inner regions might behave as dynamical attractors, whose phase-space density is nearly invariant under the accretion of collisionless matter (Gao et al. 2004; Kazantzidis, Zentner & Kravtsov 2006). In this scenario, one might expect less structural evolution of the inner regions of massive ETGs at $z < 1$, compared to models in which most gas had not yet turned into stars before the mass assembly of their inner regions took place. Hence, one way to study the formation scenario of massive elliptical galaxies is to quantify the evolution of the mass distribution in their inner regions in the redshift range $0 < z < 1$.

Over the last few decades, tremendous progress has been made in our understanding of cosmic structure and galaxy formations mechanisms. This is in part due to (semi-)analytic galaxy-formation theory giving us detailed calculations of the CDM power spectrum (Peebles 1982; Blumenthal et al. 1984), Press–Schechter theory (Press & Schechter 1974), the statistics of peaks in Gaussian Random fields (Bardeen et al. 1986), and galaxy formation models (White & Rees 1978). Analytical approaches have their limitations though in addressing more complicated physical processes. In the absence of precise analytical methods for computing for example the non-linear dark matter (DM) power spectrum, the properties of DM substructure, etc., full-scale numerical simulations are the only method available. Semi-numerical models have also been employed, building on numerical simulations. The combined results of these semi-analytical and numerical simulations have provided valuable insight into the study of galaxy formation over the last two decades (Frenk et al. 1999; Springel, Di Matteo & Hernquist 2005a; Springel et al. 2005b; Springel, Frenk & White 2006; Schaye et al. 2010; Springel 2010; Vogelsberger et al. 2012, 2014; Schaye et al. 2015).

Strong gravitational lensing due to ETG provides a robust observational test of a number of theoretical predictions for galaxies at $z \leq 1$, especially when it is being combined with stellar kinematic data (Sand et al. 2004; Treu & Koopmans 2004; Koopmans et al. 2006). Employing the results of the lens models (Koopmans et al. 2006), some studies (Treu et al. 2006) quantified the degree of homogeneity in the inner density profiles of the ETGs, suggesting close to isothermal density profiles on average, but with a scatter. Many questions however remain unanswered. To study strong-lensing ETGs in more detail, the Sloan Lens ACS Survey (SLACS; Bolton et al. 2006; Koopmans et al. 2006; Treu et al. 2006; Gavazzi et al. 2007; Bolton et al. 2008a; Gavazzi et al. 2008; Auger et al. 2009, 2010a,b; Treu et al. 2009; Newton et al. 2011; Shu et al. 2015, 2017) and the Strong Lensing Legacy Survey (SL2S; Ruff et al. 2011; Gavazzi et al. 2012; Sonnenfeld et al. 2013a,b, 2015) have provided relatively uniform samples. The lens models from these surveys, however, have not yet been compared in detail to high-resolution numerical simulations. An exception is Bellagamba, Tessore & Metcalf (2017) who found a significantly shallower slope for the DM alone by preforming a detailed study of one lens.

In this paper, we present a new lens-galaxy simulation and analysis pipeline using the Evolution and Assembly of GaLaxies and their Environment (EAGLE) simulations (Crain et al. 2015; Schaye et al. 2015) and compare the results from mock lens projections to those of SLACS and SL2S. We introduce an automatic prescription that creates, models, and analyses simulated lenses. We introduce a weighing scheme necessary to reduce the selection bias and statistically compare the simulated lenses with observations. We also probe the systematic errors and biases arising from the different line-of-sight projections and environmental effects. We find that using a simplex parameter estimator, we can quite robustly obtain the key lensing observables, e.g. the Einstein radius and mass density slope, etc. We put forward the concept of a 2D-complex space involving axial ratio and position angle in order to disentangle the degeneracy among them.

The paper is structured as follows. In Section 2 we summarize the EAGLE galaxy formation simulations and the relevant codes that we use in this paper. Section 3 describes the simulation and analysis pipeline that we have constructed. Lens modelling details are explained in Section 4. The results of our mock-lens analyses are described in Section 5. We compare our mock-lens samples and their properties with observations in Section 6 and conclude with a summary in Section 7. Throughout the paper we use EAGLE simulations that assume a Chabrier stellar initial mass function (Chabrier 2003). The values of the cosmological parameters are $\Omega_\Lambda = 0.693$, $\Omega_b = 0.0482519$, $\Omega_m = 0.307$, $h = H_0/(100\,\mathrm{km\,s^{-1}\,Mpc^{-1}}) = 0.6777$, and $\sigma_8 = 0.8288$. These are taken from the Planck satellite data release (Planck Collaboration XVI 2014), again in agreement with the EAGLE simulations.

2 NUMERICAL CODES

In this section we briefly describe the simulations, numerical codes, and tools that are used in this work. We describe the EAGLE hydrodynamical simulations from which we select lens galaxies (Section 2.1), the GLAMER ray-tracing code to simulate mock lenses for various lens orientations and sources (Section 2.2), and the LENSED lens-modelling code used to infer mass-model parameters (Section 2.3).

2.1 Galaxy-formation simulations from EAGLE

EAGLE[1] is a suite of hydrodynamical simulations of the formation of galaxies and supermassive black holes in a ΛCDM universe (Crain et al. 2015; Schaye et al. 2015; McAlpine et al. 2016). EAGLE simulations are carried out using the modified *N*-Body Tree-PM (particle mesh) SPH (smoothed particle hydrodynamics) code GADGET 3 (Springel et al. 2005b). The resulting galaxies are in good agreement with observations of the star formation rate, passive fraction, Tully–Fischer relation, total stellar luminosity of galaxy cluster and colours (Schaye et al. 2015; Trayford et al. 2015), the evolution of the galaxy stellar mass function and sizes (Furlong et al. 2015, 2017), rotation curves (Schaller et al. 2015a), and the α-enhancement of ETGs (Segers et al. 2016).

The subgrid physics employed in EAGLE is based on that developed for OWLS (Schaye et al. 2010) and used also in GIMIC (Crain et al. 2009) and cosmo-OWLS (Le Brun et al. 2014). The modifications to the SPH implementation together are known as 'Anarchy' (Schaller et al. 2015b). EAGLE galaxies are defined as

---

[1] http://icc.dur.ac.uk/Eagle/

gravitationally bound subhaloes identified by the `subfind` algorithm (Springel, Yoshida & White 2001; Dolag et al. 2009). The gravitational softening is summarized in Table 1.

In this paper we have chosen to use the `Reference` model having L050N0752 (see Table 1 and Crain et al. 2015; Schaye et al. 2015) to ensure that we have a coherent sample of galaxies that have been formed from an identical set of initial conditions subjected to different physical models when comparing results between different model variations of EAGLE (Crain et al. 2015) in forthcoming papers. For detailed descriptions on the various galaxy-formation prescriptions and subgrid physics we refer to Schaye et al. (2015) and Crain et al. (2015).

2.2 Strong lens simulations with GLAMER

GLAMER[2] is a ray-tracing code for the simulation of gravitational lenses (Metcalf & Petkova 2014; Petkova, Metcalf & Giocoli 2014). The deflection angles, shear, and other relevant properties are calculated using a modified tree algorithm described in Barnes & Hut (1989). It uses adaptive mesh refinement in ray-casting, based on the requirements of the source size, location, and surface brightness distribution and to find critical curves and caustics. Ray paths are determined from the observer to the source plane through multiplane deflection, convergence, and shear calculations. GLAMER allows for a wide variety of source types and the mass distribution on each lens plane can be represented in several different ways, for example via a surface density map in FITS format. The resulting lensed images are subsequently convolved with a point spread function (PSF) and appropriate noise levels can be added. For further details one can consult GLAMER I and II papers (Metcalf & Petkova 2014; Petkova et al. 2014).

In this paper, we use a single lens plane for representing the convergence of galaxies extracted from EAGLE, because the maximum box size (<100 Mpc) is still small compared to the cosmological distances involved. This can be expanded to multiple lens planes for much larger boxes. We also assume an elliptical Sérsic profile for the sources with varying parameters, placed inside the diamond caustic to generate preferentially highly magnified systems, similar to those found in the SLACS and SL2S surveys. All of these choices can be varied in the pipeline if desired.

2.3 Gravitational lens modelling with LENSED

LENSED[3] is a publicly available code which performs parametric modelling of strong lenses by taking advantage of the massively parallel ray-tracing kernel on a graphics processing unit (Tessore, Bellagamba & Metcalf 2016) to perform all necessary calculations. Combining these accurate and fast forward simulations with the Nested-Sampling Bayesian analysis, MULTINEST (Feroz & Hobson 2008; Feroz, Hobson & Bridges 2009; Feroz et al. 2013), allows the simultaneous optimization of tens of non-linear parameters of the selected model (e.g. lens and source) and the full posterior probability distribution for the mass distribution and the background source in typically 10 min on a multicore machine. The setup of the physical system, priors, input files including images, masks, PSFs, and noise maps can be done using a single configuration file. The code reports statistically well-justified errors, including degeneracies, for the lens model parameters, i.e. the full posterior

reconstruction, and also simultaneous fitting of sources and lenses. LENSED has been well tested on SLACS lenses. For details see Tessore et al. (2016) and Bellagamba et al. (2017).

3 PIPELINE

In this section we describe the SEAGLE (Simulating EAGLE LEnses) pipeline in more details. We describe the selection criteria of the lens candidates from EAGLE (Section 3.1), the lens galaxy extraction technique (Section 3.2), the line-of-sight projection effects on the shape of lens galaxies (Section 3.3), the method to create mock lens systems with GLAMER (Section 3.4), the automatic mask creation process (Section 3.5), and details of the final lens sample used in this paper (Section 3.6). The simulation and analysis pipeline is shown in Fig. 1.

In this paper extraction of galaxies is done at one particular redshift and the resulting mass distribution is projected along one of the three principal axes of the simulation box. A Sersic (1968) source is then placed at a random source position within the diamond caustics at a higher redshift as experimented with GLAMER. The PSF and noise are similar to those for a single orbit *HST* ACS-*F*814*W* observations to make the mock lenses appear similar to observed SLACS lenses. The resulting lenses are subsequently modelled and analysed by comparing their ensemble properties with those from SLACS and SL2S. We note that most of the above choices can be easily modified.

3.1 Lens-galaxy selection

The next generation of lens surveys [for example with *Euclid* (Laureijs et al. 2011)] are expected to increase the number of lenses by orders of magnitude, in particular finding lower mass and smaller image separation lenses. This will increase the parameter space of strong lenses in terms of their mass, stellar velocity dispersion, and other observables considerably. The selection criteria for extracting galaxies from EAGLE, however, are based on parameters obtained from currently confirmed strong lenses due to ETGs, in particular from SLACS. Keeping this restriction in mind, we explore a volume-limited sample of lens galaxies with observables (e.g. stellar mass) in the range of ETGs from SLACS (Auger et al. 2009, 2010a,b) and SL2S (Sonnenfeld et al. 2013a,b). The SLACS sample consists of a wide ranges of photometric and spectroscopic measurements using *HST* and SDSS and inferred data products, which include for example, the parameters inferred from lens modelling and stellar-population analysis (Auger et al. 2010b). The parameter space of SLACS broadly overlaps with SL2S lenses, which makes it useful to compare properties of simulated lenses with both samples.

The initial selection is based on lens redshift (z_1) and stellar mass ($M_\star$) in accordance with Auger et al. (2010a), where the lens redshift range is $0.1 \leq z_{lens} \leq 0.3$ and the stellar mass threshold is $M_\star \geq 1.76 \times 10^{10}$ M$_\odot$. No upper limit is set. The stellar velocity dispersion (σ) and half mass radii (R_{50}), which is a proxy for effective radii (R_{eff}) in observations, are only used to clip outliers, e.g. due to halo stars, mergers, and other contaminations arising from stray particles in the simulations. Table 2 summarizes the details of our selection criteria.

We find it difficult to implement an automated recipe for the lens modelling for galaxies with stellar masses, $M_\star < 10^{11}$ M$_\odot$. This is due to the resolution effect of the particles during projection, which creates prominent but artificial images in the central regions of the lenses after ray tracing, which are not seen in real lens galaxies. In order to implement an automated lens modelling scheme with

Table 1. The main EAGLE simulations. From left to right: simulation name suffix; comoving box size; number of DM particles (initially an equal number of baryonic particles are present); initial baryonic particle mass; DM particle mass; comoving Plummer-equivalent gravitational softening length; maximum proper softening length (reproduced from Schaye et al. 2015). Throughout the paper proper kpc is used synonymously with kpc unless otherwise mentioned.

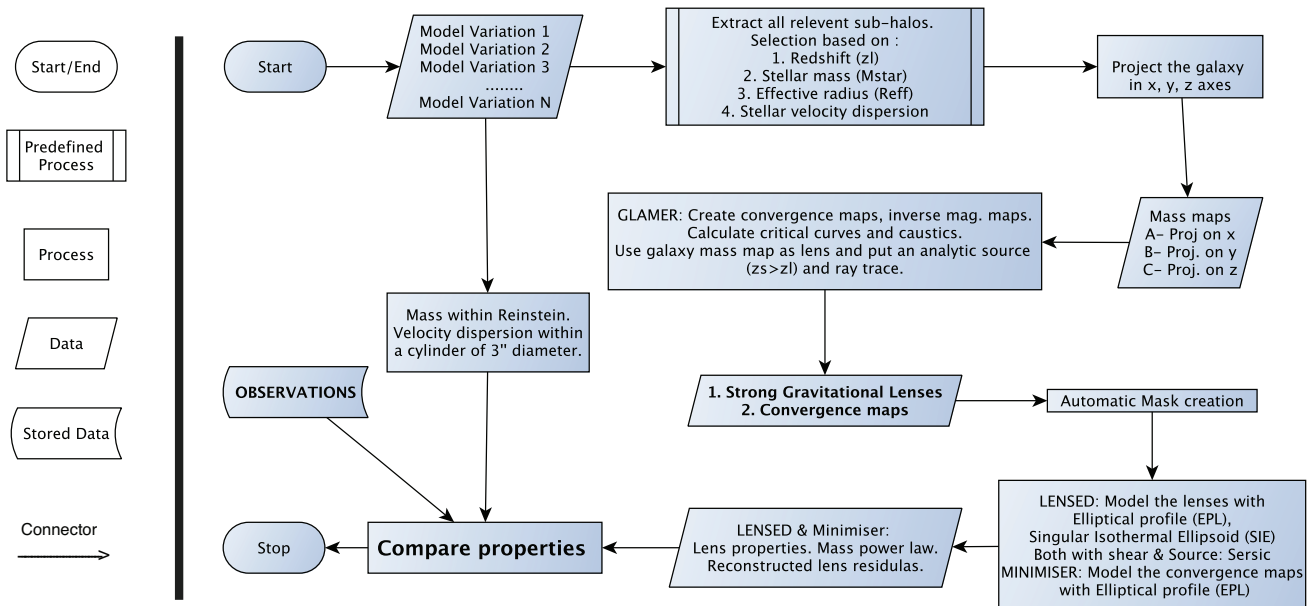| Name	L (cMpc)	N	m_g (M$_\odot$)	m_{DM} (M$_\odot$)	ϵ_{com} (ckpc)	ϵ_{prop} (pkpc)
L025N0376	25	376^3	1.81×10^6	9.70×10^6	2.66	0.70
L025N0752	25	752^3	2.26×10^5	1.21×10^6	1.33	0.35
L050N0752	50	752^3	1.81×10^6	9.70×10^6	2.66	0.70
L100N1504	100	1504^3	1.81×10^6	9.70×10^6	2.66	0.70

Figure 1. The SEAGLE flow chart showing that the convergence mass maps – simulated using GLAMER and galaxies extracted from EAGLE – are analysed via two different channels, i.e. via the modelling of the simulated lensed images, and via direct fitting of the same (lens) mass model to the convergence mass map. The two resulting parameter sets are compared to each other and to the corresponding observables coming from the SLACS and SL2S surveys.

LENSED, we therefore further restrict ourselves to galaxies with $M_\star > 10^{11}$ M$_\odot$ (calculated within a cylinder of 1.5 arcsec. in radius, consistent with SLACS) which produce extended arcs and rings (see Fig. 3). These are far less affected by any resolution effect and are still within the upper mass range of SLACS and SL2S lenses. To down-weight lower mass galaxies in the volume limited set of EAGLE lenses in comparisons to SLACS or SL2S, in Section 6.2 we introduce a weighting scheme based on their lensing cross-section, that compensates for the observational selection biases and allows for a more accurate comparison between the simulations and the observations. We ignore the magnification bias, which we assume to vary more slowly with galaxy mass unlike the cross-section.

3.2 Galaxy/halo extraction

To extract a galaxy from the EAGLE snapshots, we use the Friends-Of-Friend (FoF) catalogues. We use the stellar mass catalogue from the snapshots and particle data at the desired redshift of the currently used Reference simulation (i.e. L050N0752). The choice of aperture is important given its direct effect on the stellar mass calculation for massive and extended galaxies with $M_* > 10^{11}$ M$_\odot$ (see Schaye et al. 2015). Given that most lens-galaxies have half-mass radii of 5–10 kpc, we choose a 10-kpc aperture to select the closest analogues to observed lenses from the simulations. We select all subhalo indices that match our selection criteria, and reject

any galaxy having half-light radii <1 kpc in the EAGLE catalogues (these objects are misidentified galaxies and lie far from the Fundamental Plane). This aperture size avoids inclusion of spurious stellar mass which would be discounted in the modelling of observed lens galaxies using, e.g. a smooth Sérsic profile. Eagle catalogues have GroupNumber and SubGroupNumber which are numbers assigned to FoF group and subgroup, respectively. They are numbered according to their decreasing masses. That means subgroup 0 of an FoF group corresponds to the most massive subgroup within the group. We read the GroupNumber and Sub-GroupNumber using the same indices to recover the FoF group ID and Subfind subgroup ID and subsequently select all their particles and obtain their meta-data from the simulations, using the group IDs. Galaxy selection and outlier rejection are currently fully automated in the pipeline and the criteria can be altered if necessary.

3.3 Line-of-sight projection

Once the catalogues of DM, stellar, gas, and black hole particles of a galaxy have been extracted from the simulations, we allow for any arbitrary spatial rotation. We rotate particle position vectors around the centre of the lens galaxy. Although this does not lead to an independent lens galaxy, it does allow for some testing of the effects of orientation on the inference of the galaxy properties.

Table 2. The summary of the current SEAGLE pipeline settings.

| Observable	Value	Comments
	Galaxy selection	
$M_\star$	$\geq 1.76 \times 10^{10}\,\mathrm{M_\odot}$	Stellar mass lower threshold. Taken from Auger et al. (2010a)
σ	$> 120\,\mathrm{km\,s^{-1}}$	Stellar velocity dispersions are kept lower than SLACS
R_{50}	$> 1\,\mathrm{kpc}$	Half mass projected radius
$M_\star$	$> 10^{11}\,\mathrm{M_\odot}$	Stellar mass lower cut-off for comparison with observations
	Lens candidates	
Object properties	Value	Comments
Sim. used	Reference (L050N0752)	50 cMpc box is best for comparing with other scenarios
Orientation	x, y, and z axis	Projected surface density maps are made along each axis
Redshift	$z_l = 0.271$	Consistent with SLACS' mean lens-redshift of 0.3
No. of galaxies	252	Total number of galaxies satisfying our selection criteria
No. of projected galaxies	756	Total number of galaxies after projection on three axes
	Source properties	
Parameters	Value	Comments
Source type	Sérsic	Consistent with analysed SLACS lenses (Newton et al. 2011)
Brightness	23 apparent mag.	"
Size (R_{eff})	0.2 arcsec	"
Axial ratio (q_s)	0.6	"
Sérsic Index	1	"
Redshift	$z_s = 0.6$	"
Position	Random within caustics	Producing more rings and arcs lens systems, consistent with SLACS
	Instrumental settings	
Parameters	Value	Comments
PSF	Gaussian, FWHM = 0.1 arcsec	–
Noise	*HST* ACS-*F*814*W*, 2400 s	–
	Image properties	
Map used	Properties	Value
Surface density	(a) Size	512×512 pixels
	(b) Units	kpc
κ, Inv. mag. map and Lens	(a) Size	161×161 pixels
	(b) Units	degrees (converted from arcsec)
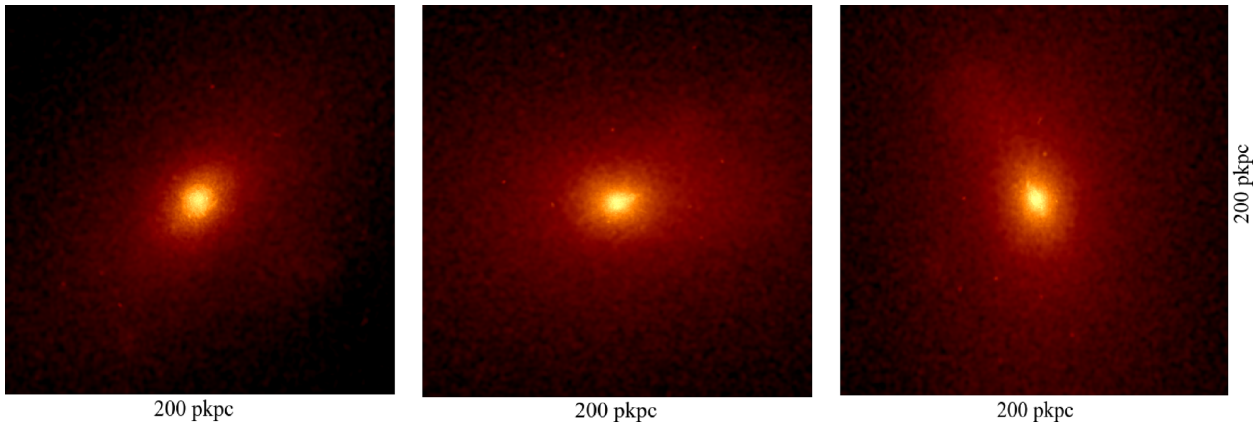
Figure 2. An example of mass maps of a typical ETG of stellar mass $= 1.9 \times 10^{11}\,\mathrm{M_\odot}$ at $z = 0.271$, extracted from the Reference (L050N0752) EAGLE simulation and the box size is 200 pkpc. Frame [left] is the visualization of projected mass map of the galaxy having axial ratio, $q \approx 0.76$ when the line of sight is rotated by (90, 0, 0) deg, i.e. 90 deg rotation in x axes with respect to the centre of the simulation box. Frame [middle] displays the galaxy having $q \approx 0.72$ when our focus has been rotated by (0, 90, 0) deg, i.e. 90 deg rotation in y axes. Frame [right] displays the galaxy with $q \approx 0.69$ when the rotation angle is (0, 0, 90) deg in z axes.

Fig. 2 shows how the projected shape of a galaxy changes when viewing it from three different angles. In this paper we use each galaxy three times, projected along each of the three principle axes of the simulation box. In the future papers we use these to assess systematics due to projection of the main galaxy halo and line-of-sight effects in the nearby environment of the lens (i.e. inside the box). The particles are then converted into projected mass maps

after smoothing of the particles with the same SPH kernel as used in the simulation (for details see appendix A of Trayford et al. 2017). Fig. 4 shows an example of simulated and modeled strong lens.

We also simultaneously calculate the surface density profiles of the matter distribution for each projected mass map. The surface densities for individual particle types (DM, stars, and gas) and a total mass profile are calculated separately. Fig. 5 shows a typical
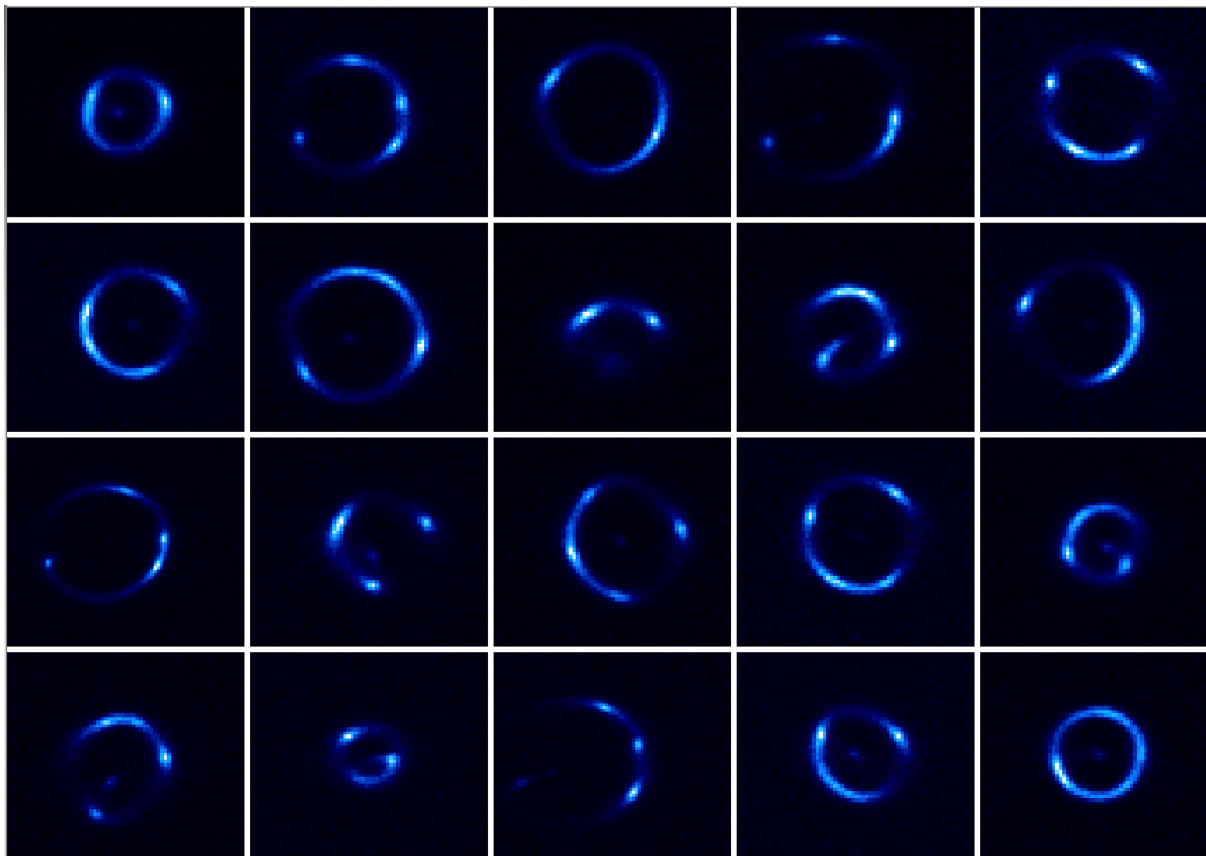
Figure 3. A subset of strong lenses from EAGLE (Reference model) 50 cMpc, $z_1 = 0.271$. Even some of the rare SLACS lenses have been mimicked very well via our pipeline. The sub-kpc fluctuations however cannot be simulated with a simple Sérsic source object. But that is not necessary for having a statistical sample of simulated SLACS like lenses. We have not put the lensing galaxy in the foreground so there is no contamination of the light from the foreground ETG.
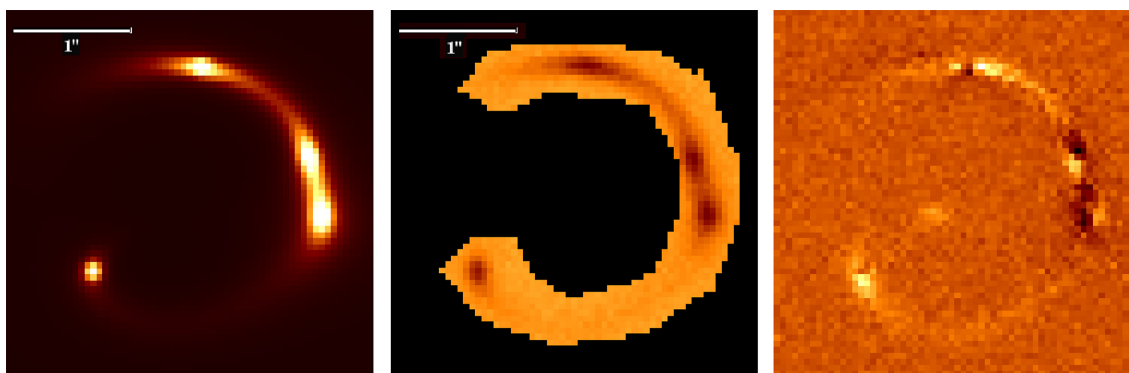

Figure 4. The left-hand panel shows an example of a simulated lens with noise and PSF (see Table 2 for details). The middle panel shows the reconstructed image of the lens inside the mask, using LENSED. The right-hand panel shows the unnormalized residual image of the data minus the model. The peak brightness of simulated lens and residuals are 1.30 and 0.37, respectively.

example for an ETG's mass profiles. The effect of the resolution of the simulation inside ∼1 kpc is clearly visible.

The resolution of the simulation plays a role in the core of the galaxy, where we hit the resolution limit (see Appendix A). 2–3 times the gravitational softening length, which is independent of the density, away from the core, its effect no longer plays a crucial role. So we mask the central pixels in the lensed images. In Section 3.5 we describe this in details.

3.4 Mock lens-system creation

The surface density maps are created on grids of 512×512 pixels (Table 2), in units of solar mass per pixel, and form the input to GLAMER. The width (100 pkpc) and pixel scale (0.2 pkpc) of the grid ensure the surface density map and corresponding convergence map are well-resolved in the relevant regions (see Tagore et al. 2018), down to the softening length and consistent with SLACS resolution of 0.05 arcsec (at $z = 0.271$, SLACS resolution corresponds to

≈0.2 pkpc). We then choose a lens and source redshifts for GLAMER to convert these mass maps into convergence maps. For each mass map, the critical curves and caustics are calculated to determine where a source has to be placed in order to create multiple lensed images. In this paper we use an elliptical Sérsic brightness profile of the source with index $n = 1$. Its apparent magnitude is constant at 23 in the *HST*-ACS *F*814*W* filter (AB system) and its redshift is $z_s = 0.6$. The other parameters are its effective radius of 0.2 arcsec, a position angle $\phi_s = 0$ deg, and a constant axial ratio $q_s = 0.6$. Given that source and galaxy position angles are uncorrelated, this fixed position angle of the source does not reduce generality. The source is placed randomly inside the diamond caustics of the lens. The pixel scale is 0.05 arcsec, and the PSF and noise correspond to an *HST*-ACS-*F*814*W* exposure of typically 2400 s. The resulting images have a size of 161×161 pixels of 8.0 arcsec. The above parameter values are currently fixed for each lens, but are typical for the sample space of SLACS lenses (Koopmans et al. 2006; Newton et al. 2011; Bandara et al. 2013). Since our goal is to assess global properties of the lenses, the precise choice of the source model (which is an exponential disk here; Sérsic with $n = 1$) is currently of secondary importance. The images are exported in standard fits-file format. Table 3 lists all parameter values. We like to point out that in this work, only arcs and rings lenses are simulated. No two image systems are simulated since the number counts of two image system in SLACS is 6/84 ∼ 7 per cent (Auger et al. 2010a) and 3/56 ∼ 6 per cent in SL2S (Sonnenfeld et al. 2013a) are very low and no evidence of the lens properties being a function of lens geometry is reported (Auger et al. 2010b; Sonnenfeld et al. 2013b). So we assume non-inclusion of the two image lenses is highly unlikely to bias the overall statistics.

In addition to the simulated lenses, we store convergence maps and inverse magnitude maps of each lens galaxy. The brightness distribution of the lensing galaxy is not added to the lensed image grid. We assume that subtraction of the surface brightness distribution of the lens galaxy can be done to sufficient accuracy so that it does not affect the analysis in the current paper. Hence we assume little covariance between the source and lens brightness distributions. Experience with high-resolution *HST*-quality data of lenses in the *I* band confirms this, although this assumption might not hold for lower resolution ground-based data.

3.5 Mask creation

The strong lens systems created using GLAMER are modelled similarly to a real lens system. Masks are generated automatically in order to enable direct comparison with the lens models to the region around the lensed images. We do this for each lens by convolving the noisy lensed images with a Gaussian with an FWHM of 0.25 arcsec to reduce the noise and smear the images to a slightly larger footprint. We then set a surface brightness threshold for the mask being a factor of typically 2.5–5 below the original noise. Pixels above the threshold are set to one and all others to zero. The mask then traces the surface brightness of the lensed images well below the noise level. We set the threshold values such that the mask bounds the significant surface brightness pixels but leaves a padding area that is largely noise example, middle panel of Fig. 4. The central 7×7 pixels are also masked to remove any artificially bright central images as a result of the finite size of the SPH kernel and limited resolution. The final mask is used in the modelling and minimizer fitting in the following steps.

3.6 The lens samples

In this subsection we summarize the pilot sample selected for this paper. Out of the 252 initially selected galaxies (Table 4), 48 have $M_\star > 10^{11}\,\mathrm{M}_\odot$. The projected stellar masses are calculated within a cylinder of 3 arcsec diameter (see Auger et al. 2010b) to keep the comparison consistent with SLACS (see Fig. 1). From the remaining galaxies having $M_\star < 10^{11}\,\mathrm{M}_\odot$, we randomly select 11 galaxies motivated to test the performance of the pipeline. We perform lens modelling on these two sets of samples. Given the pilot nature of the sample when comparing properties (e.g. total density slope) with observations we restrict to galaxies having $M_\star > 10^{11}\,\mathrm{M}_\odot$, also most reliable and least affected by SPH smoothing. To limit computation effort, we also currently only use one of the projected mass maps. The selected lenses cover nearly 1 dex in stellar mass of the SLACS, but because of the limited volume of the simulations, they are poorly represented when approaching very massive ETGs. Finally we apply the end-to-end pipeline on the sample and analyse the results in this work. The result is that 34 out of 48 lenses having substantial arcs or Einstein rings (see Fig. 3), converged to optimized solutions. 14 lenses having smaller arcs and more complex structure failed to converge to any reasonable solution in lens modelling. Table 4 summarizes the sample selection.

The reason for our current down selection of the total sample is mainly due to the complexity in the implementation of automated lens modelling with LENSED. All the resulting mass maps, inverse magnification maps, convergence maps, the simulated lenses, and model-fitting results are stored in a MySQL[4] database, which has been widely used in astronomy (Lemson & Springel 2006).

4 LENS-SYSTEM MODELLING

Once we have created all the inputs to simulate mock lens systems including observational effect and masks, we model each lens system with LENSED (Tessore et al. 2016) using either an elliptic power law (EPL; Tessore & Metcalf 2015) or a singular isothermal ellipsoid (SIE; Kormann, Schneider & Bartelmann 1994) mass model, including external shear. A total of 14 and 15 parameters are sampled for the SIE and EPL models, respectively, and posterior distributions of all lens and source parameters are created via the MCMC method nested sampling (NS).

4.1 Mass models

Various observational studies find that the EPL mass model (including the SIE) in general provides a good approximation of the mass model of massive galaxy-scale strong gravitational lenses (Treu & Koopmans 2004; Koopmans et al. 2006, 2009; Newton et al. 2011). As a first step we therefore model the lenses as an SIE plus external shear with the prior settings tabulated in Table 3. The dimensionless surface mass density of the SIE model is given by

$$\kappa(R) = \frac{b}{2R}, \qquad (1)$$

where b is approximately the Einstein ring radius and R is the elliptical radius defined by

$$R = \sqrt{qx^2 + y^2/q}, \qquad (2)$$

where q is the axial ratio (short over long axis length) and x, y are Cartesian coordinates of the model. Similarly we model and

---

[4] http://www.mysql.com/products/community/

Table 3. The prior settings used in the lens modelling with SIE + shear and EPL + shear mass model in LENSED.

Priors used in LENSED[a]

Parameter	Prior type[b]	Prior range				Description
		μ	σ	min	max	
		Elliptical power law (EPL) + shear				
x_L	norm	80.0	5.0	–	–	Lens position: x coordinate
y_L	norm	80.0	5.0	–	–	Lens position: y coordinate
r_L	unif	–	–	5.0	70.0	Einstein radius in pixel units
t_L	norm	1.1	0.1	–	–	Surface mass density slope
q_L	unif	–	–	0.2	0.99	Lens axial ratio
ϕ_L	unif	–	–	0.0	180.0	Lens position angle in degrees, wrapped around
γ_{1L}	norm	0.0	0.01	–	–	Shear vector
γ_{2L}	norm	0.0	0.01	–	–	Shear vector
x_S	norm	80.0	30.0	–	–	Source position: x coordinate
y_S	norm	80.0	30.0	–	–	Source position: y coordinate
r_S	unif	–	–	0.1	10.0	Source size in pixel units
mag$_S$	unif	–	–	-5.0	0.0	Source magnitude, adjusted with the background magnitude[c]
n_S	norm	1.0	0.1	–	–	Sérsic index
q_S	norm	0.5	0.1	–	–	Source axial ratio
ϕ_S	unif	–	–	0.0	180.0	Source position angle in degrees, wrapped around
		Singular isothermal ellipsoid (SIE) + shear				
x_L	norm	80.0	5.0	–	–	Lens position: x coordinate
y_L	norm	80.0	5.0	–	–	Lens position: y coordinate
r_L	unif	–	–	5.0	70.0	Einstein radius in pixel units
q_L	unif	–	–	0.2	0.99	Lens axial ratio
ϕ_L	unif	–	–	0.0	180.0	Lens position angle in degrees, wrapped around
γ_{1L}	unif	–	–	-0.1	0.1	Shear vector
γ_{2L}	unif	–	–	-0.1	0.1	Shear vector
x_S	norm	80.0	30.0	–	–	Source position: x coordinate
y_S	norm	80.0	30.0	–	–	Source position: y coordinate
r_S	unif	–	–	0.1	10.0	Source size in pixel units
mag$_S$	unif	–	–	-5.0	0.0	Source magnitude, adjusted with the background magnitude[c]
n_S	unif	–	–	0.5	2.0	Sérsic index
q_S	unif	–	–	0.2	0.99	Source axial ratio
ϕ_S	unif	–	–	0.0	180.0	Source position angle in degrees, wrapped around

Notes. [a]All values are in pixels except q, γ, t_L, mag$_S$, n_S, and ϕ.

[b]norm = Gaussian (with mean μ and standard dev. σ), unif = Uniform.

[c]Source's real magnitude = background magnitude − mag$_S$, where background magnitude is flux due to background in mag arcsec^{-2}.

analyse the lenses with an EPL mass model plus external shear, whose convergence is given by

$$\kappa(R) = \frac{(2 - t_L)}{2} \left(\frac{b}{R} \right)^{t_L}, \tag{3}$$

where $0 < t_L < 2$ is the power-law density slope of the mass model and the other parameters are the same as for the SIE model. This profile can arise from a three-dimensional mass distribution, given by

$$\rho(r) \propto r^{-t}, \tag{4}$$

where $t = t_L + 1$.

The EPL model allows us to (statistically) compare the ensemble of density slopes of the simulated lenses with those from SLACS and SL2S. We note that many of the SLACS density slopes were obtained from a combined lensing and dynamics analysis, not just from lensing. The same model also allows for a comparison with the convergence model fitting in Section 4.4.

4.2 Nested sampling and priors

We compare our models to the simulations using a Bayesian approach and sample the posterior via NS (Skilling 2006; Feroz & Hobson 2008; Feroz et al. 2013). NS is a modified Markov Chain

Monte Carlo (MCMC) method that carries out the integral over the posterior probability distribution function (PDF) resulting in a value of the marginalized posterior, i.e. the evidence. As a by-product it also provides a first-order sampling of the posterior. The posteriors are used to estimate the maximum a posteriori lens parameter values, their uncertainties, as well as potential degeneracies (see Tessore et al. 2016 for more details). The lens modelling is performed semi-automatically with 200 live points, where the initial values of priors are kept such that effectively all of the lens and source parameter spaces are covered (see Table 3). The parameter space is sometimes degenerate with multiple extrema, making a straightforward sampling difficult. To avoid any catastrophic failures in the reconstructed source or lens parameters, the analysis of the mock lenses was performed by trying a range of well-motivated priors without affecting the end result too much. A combination of rather uninformative Gaussian and uniform priors was found to be optimal in our modelling analysis. The details of the prior settings can be found in Table 3. In the EPL case we used tighter priors on n_s and q_s to avoid degeneracies that would slow the convergence. All NS chains are analysed through GetDist.[5] We get posterior distributions, corner plots, and also marginalized plots for each individual source and lens

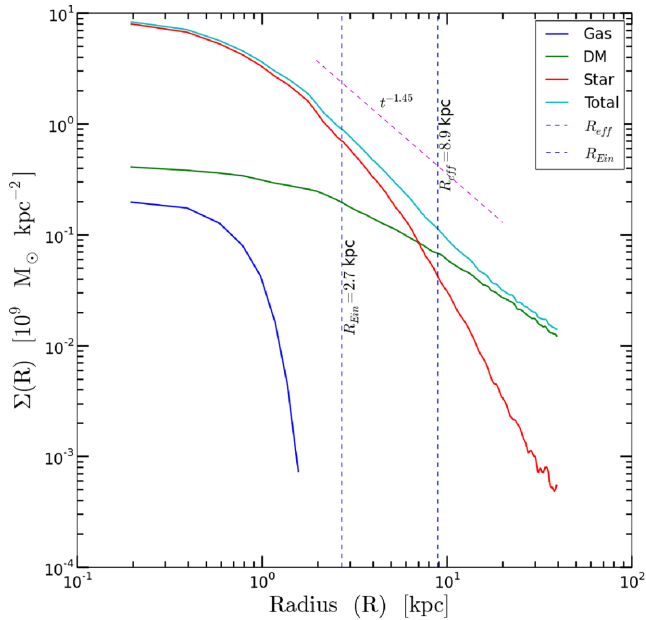[5]http://getdist.readthedocs.io/en/latest/

Figure 5. Surface density profiles of DM, stars, gas, and the total mass of a typical ETG from EAGLE. The effective radius of the galaxy and the slope of best-fitting mass model profile along with Einstein radius, as obtained from lens modelling, are also indicated.

Table 4. The sample of EAGLE lenses used.

SEAGLE-I lenses

Tag	No. of galaxies	Proj. galaxies	Comments
A	252	756	Total number of galaxies satisfying all the selection criteria (excluding $M_\star > 10^{11}$ M$_\odot$) of Table 2
B	48	144	Total number of galaxies satisfying all the selection criteria and having $M_\star > 10^{11}$ M$_\odot$
C	48	48	Number of modelled galaxies having $M_\star > 10^{11}$ M$_\odot$ using one orientation
D	11	11	Number of modelled galaxies having $M_\star < 10^{11}$ M$_\odot$ for test purposes

parameters. We tested for a range of priors for the density slopes and shear (the two main parameters of the analysis) and found that our choice of priors improves convergence and reduces the computation time. Hence we use the prior in Table 3 to speed up convergence, but they have little to no impact on the final solution. See Appendix B for details.

4.3 Choice of source model

The source parameters are observationally motivated (Bolton et al. 2008b; Newton et al. 2011) and can in principle be varied between sources. Our main goal in this paper is to infer global properties of the lensing galaxies, and the precise choice of the source model is currently of secondary importance (see Section 3.4). So even though some of the SLACS and SL2S sources show irregular morphologies, we expect a change in the source model not to bias the result especially since the systematic errors far outweigh random errors. Tessore et al. (2016) for example performed rigorous testing to

demonstrate that the choice of source model does not bias the lens-modelling (see Section 4.4 of Tessore et al. 2016). They reported only a minor variance for the lens modelling parameters. We tested with a subsample of our pilot lenses and note sometimes an increase in the computational time for some but no change in the distribution of the parameters (see Appendix B). Hence in the current paper we have decided not to change the source model parameters between lenses.

4.4 Convergence-map modelling

We also fit the EPL model in equation (3) directly to the convergence map of the galaxy inside the same mask that was used for the lens modelling, using the Nelder–Mead (NM) simplex method (Nelder & Mead 1965) including some annealing to help convergence. We do this in order to compare the resulting lens-model parameters, as discussed in Section 4, with those from the actual mass model of the simulated galaxy. Even the resulting parameters from this 'direct' fit are still a limited representation of the true mass distribution, which can be more complex than an EPL mass model. Comparing the two, however, allows us to assess the reliability of the lensing results and the variance between the two parameter sets.

We use an unweighted least square penalty function. We take the parameter values that minimize the penalty function from a set of 10 different optimization runs with random initial parameter values, each having a maximum of 150 iterations. Most solutions agree well, with some outliers due to local minima. We choose the solution with the lowest penalty from this set, in general leading to a robust solution. This step of analysis in the pipeline is important for a number of reasons: (1) we obtain a fairly robust estimate of the main observables of the lensing galaxies such as the Einstein radius, axial ratio, position angle, and density slope, (2) we can make a direct comparison with the modelled output for each individual lenses, (3) the residuals obtained via this analysis could also be used for power-spectrum analysis.

5 COMPARING THE RESULTS FROM LENS AND CONVERGENCE MASS MODELS

The two independent mass-model analyses, i.e. via lens modelling and via direct convergence-map fitting, provide a consistency check and assessment of systematic errors on the simulated lenses when compared with observations (Marshall et al. 2007). We compare the results from both model fits using an identical family of mass models. To compare their ensemble properties, however, we need to introduce a weighting scheme that mimics the selection effects in observed samples. These selection biases can be rather complex (Dobler et al. 2008) but in this paper we use the lens cross-section based on stellar mass. We ignore the magnification bias which is expected to change slowly with stellar mass for the most massive lens galaxies that we study.

Below we discuss the results from the comparison between the two sets of parameters, in particular the complex ellipticity, its correlation with external shear, and the Einstein radius. We have used the SIE model results when comparing with observations' ellipticity and position angle which is consistent with the model used in SLACS and SL2S. For comparison of density slopes we have used EPL modelling results which are also consistent with the mass density slope model used in SLACS and SL2S.

5.1 Complex ellipticity

The position angle of the lens mass model has an ambiguity of $\pm\pi$ due to its point symmetry. In addition, when the lens is nearly round ($q \to 1$), the position angle becomes ill-defined. In order to disentangle this degeneracy we use a complex ellipticity representation which connects both ϕ and q.

To accomplish this, we use the complex ellipticity defined as

$$\epsilon = \frac{(1-q)}{(1+q)} e^{+2i\phi} \, , \tag{5}$$

or in vector notation:

$$(\epsilon_1, \epsilon_2)^{\mathrm{T}} = \frac{(1-q)}{(1+q)} (\cos(2\phi), \sin(2\phi))^{\mathrm{T}} \, . \tag{6}$$

In this representation rounder lenses will have a smaller values of ϵ, regardless of the value of ϕ. For smaller values of q, the absolute value of ϵ increases and ϕ should be better determined. The agreement between two models depends on the distance in this ϵ-space, $|\epsilon_{\mathrm{model\,1}} - \epsilon_{\mathrm{model\,2}}|$.

We present the model values of ϵ from both the lensing and direct fitting to the convergence maps in Fig. 6. The shear vectors from the lens model are also indicated. Calculating $\Delta\epsilon_1 = \epsilon_{1,\,\mathrm{L}} - \epsilon_{1,\,\kappa}$ and $\Delta\epsilon_2 = \epsilon_{2,\,\mathrm{L}} - \epsilon_{2,\,\kappa}$, where 'L' suffix refers to LENSED results and 'κ' suffix refers to results from convergence map fitting, we find standard deviations of 0.24 and 0.17 for $\Delta\epsilon_1$ and $\Delta\epsilon_2$, respectively. The errors on the standard deviation are 0.1 and 0.07, respectively, hence the differences in the two directions are not significant. The scatter is significant though. We conclude that for lower stellar mass lenses ($M_\star < 10^{11}\,\mathrm{M_\odot}$) a significant difference can exist between the inference of the complex ellipticity from the convergence map and that from lens modelling. This might be regarded as a systematic error or bias in lens modelling which is hard to overcome. Below we investigate its cause in a little more detail.

5.2 Shear versus ellipticity

For the majority of the lens systems there is a good agreement between the values of the complex ellipticity from both analyses (Fig. 6, for errors see Section 5.1), but some systems suffer from a significant mismatch. Some previous studies have associated the differences in alignment and ellipticity to the presence of external shear (complex γ), given by

$$\gamma = \gamma_1 + i\gamma_2 \, . \tag{7}$$

They also indicated a pronounced degeneracy between ellipticity and external shear (Bandara et al. 2013; Tessore et al. 2016). We find that the majority of the systems with large differences in the complex ellipticity between the lens and convergence modelling have external shears that have a preferred angle (Fig. 7) to the vector joining the two ϵ measurement, $\overline{\epsilon_{\mathrm{L}}\epsilon_{\mathrm{K}}}$. This correlation in ellipticity and shear angles suggests that the 'external' shear is in fact 'internal' and is possibly caused by the mass distribution of the lens galaxy and not by external galaxies. In the latter case no strong correlation between shear and ellipticity angles would be expected. Hence, contrary to Bandara et al. (2013), who suggested that there may not be a direct correlation between q and γ, we find a correlation between γ and ϵ values of our simulated lenses (Fig. 6), being

$$\gamma = 0.226\epsilon + 0.015. \tag{8}$$

Also we compute the angle (φ) between the shear vector and the line joining the complex ellipticities, ϵ_{L} and ϵ_{K}, obtained from lens

modelling and convergence ellipticity fitting respectively. Fig. 7 illustrates the normalized distribution of angle φ in degrees. It reaches peak at ~135 deg implying that the shear components γ_1 and γ_2 appear orthogonal to ϵ_1 and ϵ_2, respectively. But the standard deviation in the distribution is ~50 deg which also suggests that orthogonal orientations of the shear vector have considerable scatter.

Based on this strong correlation and the apparent alignment or orthogonality between shear and ellipticity, we conclude that much of the difference in ellipticity inferred from lens models and direct fitting to the convergence maps is the result of an internal shear causing a bias in the lens models. This shear is therefore not caused by the external galaxies, but more likely by a difference between the assumed mass model (SIE) and the true mass model. Its difference is likely compensated for by the shear used in lens modelling. A first-order deviation could be boxy or diskines of the galaxy.

5.3 Einstein radius

Another comparison between the two models is that between the inferred Einstein radii. We have to be careful here though since the lens model that we use is a singular mass model whereas the convergence is affected by the SPH kernel and therefore has a small (0.7 kpc) core that might affect a direct comparison. Fig. 8 shows the comparison of the Einstein radii obtained from the convergence and the lens modelling. The values obtained from the two independent analyses agree reasonably well and without an appreciable bias, but there is a large ~20 per cent scatter (shaded region) from the one-to-one line. We rejected four data points which have a difference of more than 0.5 arcsec as critical failures that can heavily bias the standard deviation. From individual inspection of the first, we find that the Einstein radii from the lens models seem more reliable than from the convergence fitting, possibly due to the central core affecting a direct fit.

5.4 Density profile

Finally we describe the comparison of surface density slopes inferred via convergence fitting, t_{NM} and LENSED, t_{LENSED}, respectively. In Fig. 9, we show a normalized number density histogram of ratio of the mass density slopes analysed from both the processes. We find a mean ratio of 0.91 for $t_{\mathrm{NM}}/t_{\mathrm{LENSED}}$, with a standard deviation of 0.17. Even though the mean suggest a one-to-one correlation between the mass density slopes obtained from lens modelling and convergence fitting, from Fig. 9 we can also see a tail suggesting that some differences are still present in them. These differences can be attributed to the different methodologies used in direct fitting and lens modelling. The lens modelling fits the density profile (more precisely that of the potential) near the lensed images, whereas the direct fit is mostly fitting the higher density regions inside the mask. The overall agreement however is encouraging, suggesting that lensing does not provide strongly biased density slopes.

6 COMPARISONS WITH SLACS AND SL2S

Having studied how well lens-model parameters agree with direct fitting of the same surface density model to the simulations, and having assessed their level of systematic and/or random differences, in this section we do a first-order comparison between EAGLE lenses from the Reference model with those from SLACS and SL2S. In the latter cases we make a correction for the lensing cross-section inferred from their stellar masses (see Section 6.2). We concentrate on lenses with a stellar mass exceeding $10^{11}\,\mathrm{M_\odot}$, which we believe
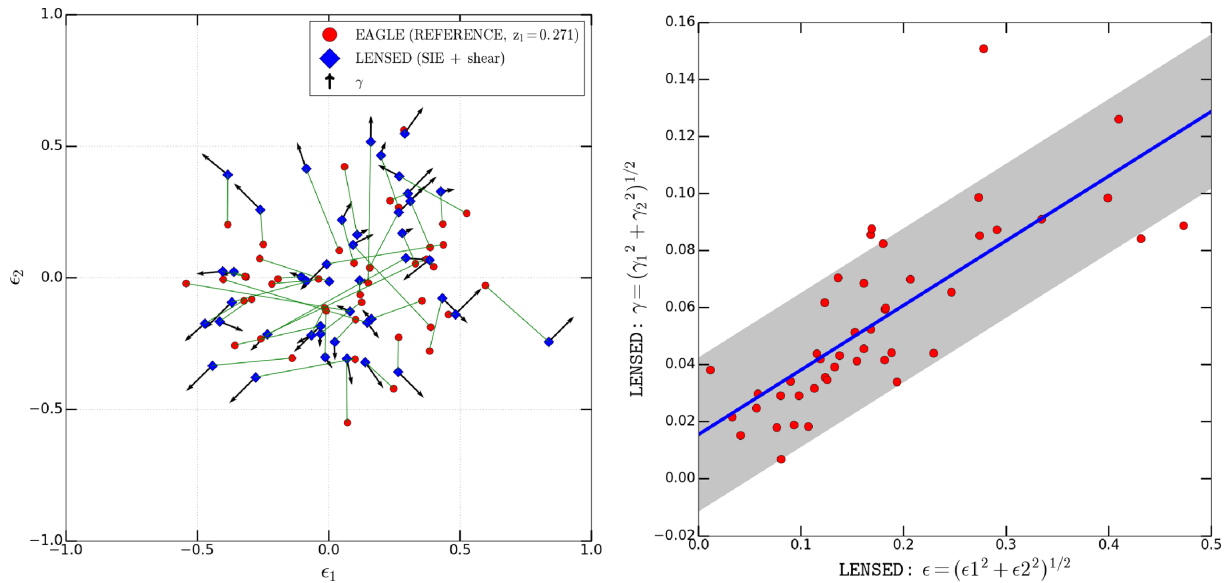
Figure 6. Left-hand panel: The complex ellipticity (see equation 6) of the SIE lens models (equation 1) from LENSED (blue diamonds) and from a direct fit to the convergence mass maps (red filled circles). The green line represents the line joining the two ϵ measurement ($\overline{\epsilon_L \epsilon_K}$), from lens modelling and direct fitting. The shear vector (γ) tends to point radially outwards in this plot, so the ellipticity is degenerate with the shear. It is most likely to cause differences in the ellipticity in the direction of the shear which causes the true lens mass model to deviate from the assumed mass models. Right-hand panel: Complex ellipticity versus shear suggests a strong correlation among them. The shaded region shows the 1σ (=0.027) interval. Here samples C and D (see Table 4) have been used.
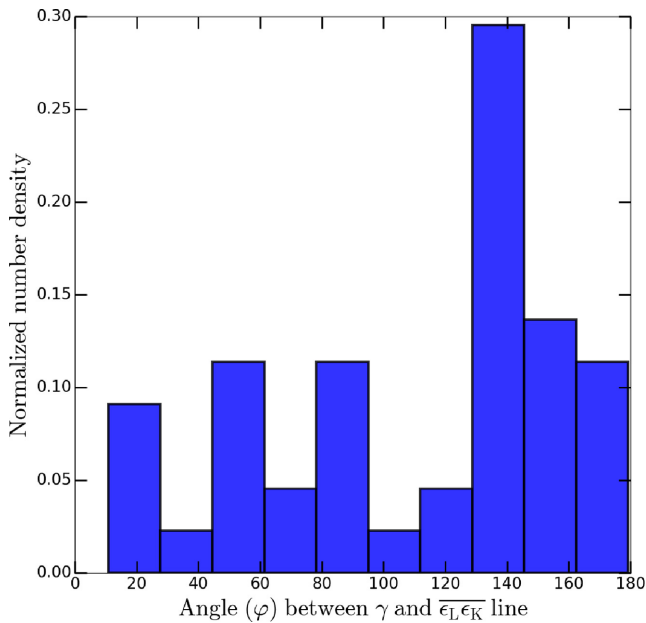
Figure 7. The normalized number density histogram of the angle (φ) between the shear vector (γ) and the $\overline{\epsilon_L \epsilon_K}$ line.

Figure 8. Comparison between the values of the Einstein radius R_{Eins} inferred from SIE lens modelling and convergence fitting. The blue line is the one-to-one correspondence. The scatter is given by the grey-shaded region. The error bars are the same 0.2 value of the scatter. Here samples C and D (see Table 4) have been used.

are currently most reliably represented in the EAGLE simulations, based on the assessments in the previous section.

6.1 SLACS and SL2S

SLACS is an *HST* snapshot imaging survey, where lens candidates were selected spectroscopically from SDSS (Bolton et al. 2006). With more than a hundred confirmed strong lens systems, SLACS is currently the largest and most complete early-type lens survey.

The SLACS candidates were selected to yield bright lenses, i.e. massive ETGs, in particular luminous red galaxies with faint star-forming background sources, generally with irregular morphology. Hence the SLACS sample was primarily a lens-selected sample. The approximate mean Einstein radius is 1.2 arcsec (Koopmans et al. 2006; Auger et al. 2010a) with background galaxies having a
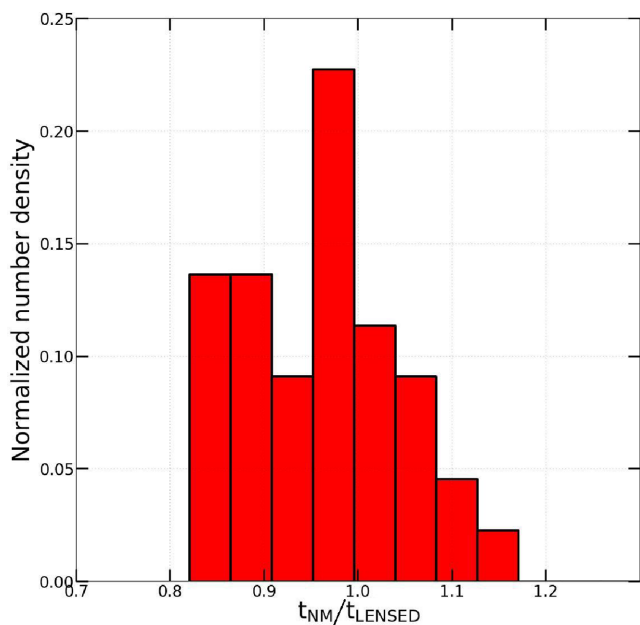
Figure 9. Comparison between the values of the mass density slope obtained from LENSED, t_{LENSED}, and convergence fitting, t_{NM}. Here samples C and D (see Table 4) have been used.

Figure 10. The mass function of galaxies having stellar masses $M_\star > 10^{11}\,M_\odot$, including and excluding the weighting scheme based on stellar mass as discussed in the text. Here sample B has been used.

typical scale length of about 0.2 arcsec (Koopmans et al. 2006). In later SLACS papers the sources were modelled with Sérsic profiles (Newton et al. 2011).

SL2S (Cabanac et al. 2007) is a survey dedicated to find and study galaxy-scale and group-scale strong gravitational lenses in the Canada France Hawaii Telescope Legacy Survey (CFHTLS). The galaxy-scale SL2S lenses are found by searching the 170 deg^2 of the CFHTLS with the automated software `RingFinder` (Gavazzi et al. 2014) looking for tangentially elongated blue arcs and rings around red galaxies. The lens candidates undergo a visual inspection and the most promising systems are followed up with *HST* and spectroscopy. For details one can consult Gavazzi et al. (2012).

SL2S differs from SLACS in the way lenses are found. While in SL2S lenses are identified in wide-field imaging data, SLACS lenses were selected by searching for spectroscopic signatures coming from two objects at different redshifts in the same line of sight in the Sloan Digital Sky Survey (SDSS) spectra. These two different techniques lead to differences in the population of lenses in the respective samples. Due to the relatively small fibre used in SDSS spectroscopic observations (1.5 arcsec in radius), the SLACS spectroscopic survey tends to limit the search to lenses with equivalent or smaller Einstein radii, where light of both the arcs from the lensed source and the deflector is captured within the fibre. SL2S however finds a larger number of lenses with Einstein radii greater than 1″, because they are more clearly resolved in ground-based images. BELLS have used the same methodology as SLACS to select the strong lenses, so they do not provide additional information on selection effect, hence they are not included in this comparison (Brownstein et al. 2012).

Fig. 3 shows a subset of simulated lens systems closely mimicking SLACS lenses (Bolton et al. 2006) in morphology and largely being arc and ring systems. Small-scale structure in the lensed images is lacking, because we are using a Sérsic source rather than the more complex (star-forming) real systems. We do not aim to repro-
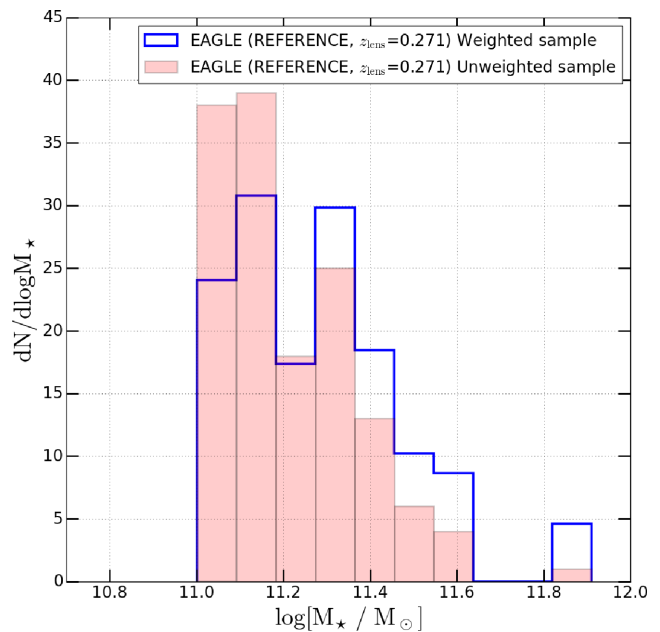
duce small-scale features in the source because we only compare global properties such as Einstein radii, axial ratios, density slopes, and position angles between SLACS and SL2S and the recovery of these quantities should not strongly depend on the fine-scale structure of the source.

6.2 Lens selection bias

The statistical comparison of a sample of volume and mass-selected lenses systems from simulations with observations is difficult due to selection biases as well as the often small simulation volumes compared to the volumes probed by lens surveys. The sample properties are for example affected by a lens cross-section that is mass dependent and a magnification bias which are different for different surveys. Because a precise analysis is beyond the scope of this paper, we only correct for the largest of these effects, being the lens cross-section. We assume that the magnification bias does not vary strongly with galaxy mass, which is a reasonable assumption if the source is small compared to the lens cross-section and if the properties of the lens mass model (besides mass) such as its flattening also do not depend strongly on mass. In most surveys that are dominated by $M_\star$ ETGs, these are reasonable assumptions.

The lensing cross-section for the EPL model that we assume (generally close to the SIE), is proportional to the square of the Einstein radius, which in turn is proportional to the stellar mass, assuming the Faber–Jackson relation (Faber & Jackson 1976) and a constant mass-to-light ratio. The latter is a direct observable in both the simulations and observations. We therefore define our weighting scheme (Fig. 10) per lens simply as

$$W(M) \equiv \left(\frac{M_\star}{\langle M_\star \rangle} \right), \tag{9}$$

with $\langle M_\star \rangle$ being the average of the sample. This scheme is used to re-weigh each strong lens when comparing distributions of parame-
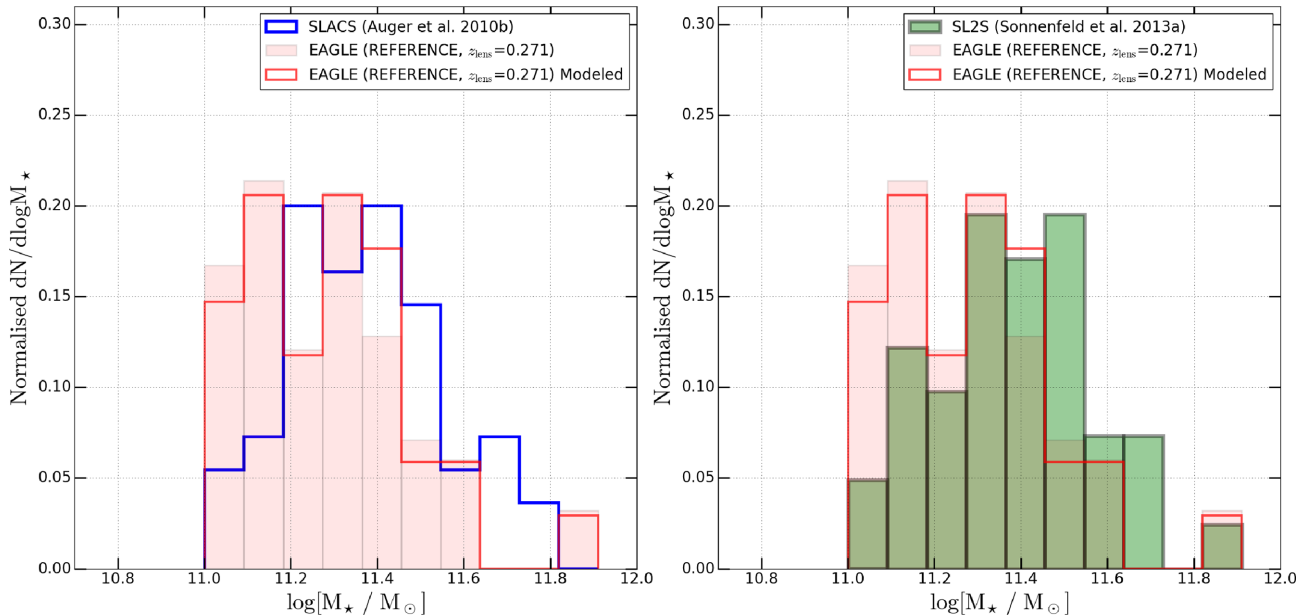
Figure 11. Comparison of the EAGLE lenses (total sample and modelled sample) with SLACS (left) and SL2S (right) lenses having stellar masses $M_\star > 10^{11}$ M$_\odot$.

ters between observed lenses (i.e. SLACS and SL2S) and simulated lenses. Because most of the lenses are drawn from the exponential tail of the mass function, even such a rather strong (linear) reweighing has only a limited impact on the tilt of the distribution functions. Fig. 10 shows that although massive ellipticals are rarer than low stellar mass galaxies, more massive ellipticals are more likely to be observed in a lens-survey because of their larger lensing cross-section.

Now we compare the properties of simulated EAGLE lenses with SLACS and SL2S. In this paper we restrict ourselves to $M_\star > 10^{11}$ M$_\odot$. Table 4 summarizes the number of galaxies, lenses, and projected mass maps. We compare the number density versus stellar mass, the mass density slope and then compare ellipticity and position angle in complex space that we mentioned in Section 5.1.

6.3 Stellar masses

In Fig. 11 we compare the simulated and observed stellar mass functions of the lens samples. Although not perfect, given the small-number statistics of the samples, the distributions show that the re-weighting scheme results in a distribution of EAGLE lenses similar to that of SLACS and SL2S. Although a significant number of EAGLE lenses are within the stellar mass range $10^{11.0-11.2}$ M$_\odot$ which are not common in SLACS and SL2S, we can still compare them considering that the simulation box covers only a fraction of the real universe and sample variance is thus very large.

6.4 Density slopes

To compare the density slopes, t (see equation 4) of the simulated lenses with their SLACS and SL2S counterparts, we have binned them into two mass ranges and one overlapping mass range: $10^{11.0-11.5}$, $10^{11.5-12.0}$, and $10^{11.0-12.0}$M$_\odot$. Fig. 12 shows the (normalized) histograms of the density slope. We find a mean value of

density slope of 2.26, which quite similar, although slightly higher than SLACS with 2.08 and SL2S with 2.16. This can be explained by several SLACS lenses having much more shallower slopes (≈ 1.6) especially in the $10^{11.5-12.0}$ M$_\odot$ stellar mass range and SL2S lenses are highly concentrated around density slope ≈ 2.10 in all the three mass-bins which makes the mean value of SLACS and SL2S density slope lower than that of EAGLE. This slight difference (although within rms limits) can be attributed to the subgrid physics, feedback mechanisms used in this simulation run, and/or due to systematics. These aspects will be tested in the forthcoming paper in this series.

The mean slope is also consistent with other studies where the mass density slopes are determined from the central dynamics of local galaxies (Dutton & Treu 2014; Tortora et al. 2014) and recent simulations (Remus et al. 2017; Xu et al. 2017). In these simulations, however, the slopes were calculated directly from the particle distributions whereas here we use lens modelling and convergence fitting. In Table 5 we have summarized the mean, root mean square (RMS), median, and the 68 per cent confidence interval for the three stellar mass bins.

6.5 Complex ellipticity

Finally, we compare the complex ellipticity from lens modelling of EAGLE lenses (Section 5.1) and SLACS. We do not use SL2S results since we do not have direct access to these mass model parameters. Fig. 13 shows the SLACS lenses in black dots and EAGLE lenses in a similar way as in Fig. 6. The grey-shaded region shows the domain of SLACS obtained from Bolton et al. (2008a). We find broad agreement between them for 33 out of 45 modelled EAGLE lenses. SLACS lenses are concentrated around the origin of the plot but still some of them suffer from the $q - \phi$ degeneracy (or 'conspiracy'), with 12 out of 45 modelled EAGLE lenses are completely outside of the shaded region (Fig. 13, left-hand panel). When comparing with SL2S lenses, we see a spread in complex ellipticity for SL2S data whereas most EAGLE lenses
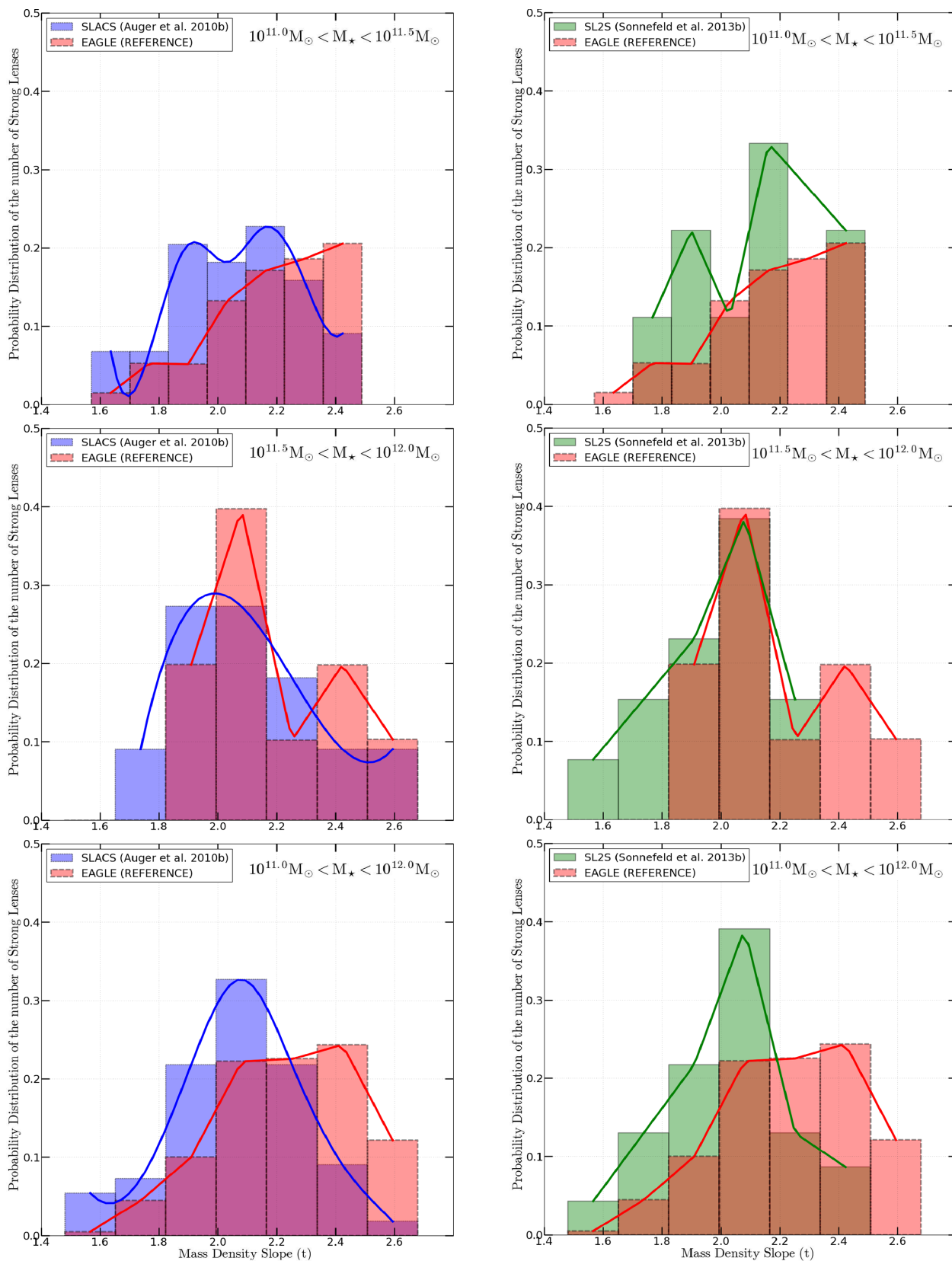
Figure 12. The probability distributions of the mass density slope (t, see equation 4) for selected lenses of Reference scenario at $z_l = 0.271$ in three stellar mass-bins of $10^{11.0-11.5}$, $10^{11.5-12.0}$, and $10^{11.0-12.0}$ $M_\odot$. They are compared to SLACS (left column) and SL2S (right column) samples. The distributions for EAGLE lenses have been weighted using equation (9). We have created a homogeneous and statistically representative sample of simulated mock strong lens systems mimicking observational surveys of SLACS and SL2S.

Table 5. The mean, rms, median, and 68% confidence limits of mass density slopes, t (see equation 4) of the simulated lenses.

$\log M_\star$ ($M_\odot$)	Mean	RMS	Median	68% CL
11.0–11.5	2.26	0.26	2.26	1.49–3.03
11.5–12.0	2.28	0.21	2.23	1.46–3.00
11.0–12.0	2.26	0.25	2.26	1.49–3.03

are well within the range. This might indicate that some of the SL2S lenses suffer from large modelling degeneracy. But also SL2S lenses reside in a group environment. So the environment of SL2S lenses can also contribute to the cause of having a much broad parameter space for axial ratio and ellipticity for SL2S lenses. The most critical case being SL2S J221326 − 000946 which is a disky system with axial ratio 0.20 and P.A. −41.5 deg (measured east of north).

7 DISCUSSIONS AND SUMMARY

In this paper we have presented an end-to-end strong-lens simulation and modelling pipeline, allowing us to assess the (dis)agreement between mass-model parameters (e.g. density slope, complex ellipticity) inferred from lens modelling and from direct fitting to the simulations, using the same mass-model family. In the current implementation (called 'SEAGLE'), we use the EAGLE (Reference-L050N0752) hydrodynamical galaxy simulations (Crain et al. 2015; Schaye et al. 2015), the GLAMER ray-tracing package (Metcalf & Petkova 2014; Petkova et al. 2014), the LENSED lens-modelling code (Tessore et al. 2016), and model all lenses as power-law elliptical mass models or singular isothermal ellipsoid mass models with external shear.

When making a stellar mass cut in EAGLE at $> 10^{11}$ $M_\odot$ and after re-weighting the EAGLE stellar mass function $dN/dM_\star$ by a simple estimator of the lens cross-section (Fig. 10), we find that the simulated lenses have a broadly similar stellar mass function to SLACS and SL2S. Their visual appearance is also strikingly similar (see Fig. 3). This motivates us to compare these observed lens samples to the simulated lens systems.

In more detail, the conclusions from this work can be briefly summarized as follows:

(1) When comparing the results from lens modelling and direct fitting of the mass surface density of lenses in the simulations, we find a correlation between the external shear (γ) and the complex ellipticity (ϵ), with $\gamma \sim \epsilon/4$ (Fig. 6). This correlation indicates a degeneracy in the mass model, where the shear compensates for a mismatch between the model and the real mass distribution. This is supported by the fact that the shear and complex ellipticity angles are correlated (Fig. 7). This could be related to a disky or boxy mass model, ill described by the elliptical model in the direct fit, but affecting the lensed images.

(2) The Einstein radii of the lens models and direct fits broadly match, i.e. within a 20 per cent scatter (Fig. 8). We attribute this surprisingly large scatter due to the fact that lens modelling really only fits the density profile (more precisely that of the potential) near the lensed images, whereas the direct fit is mostly fitting the higher density regions inside the mask, which might lead to a larger scatter when inferring the Einstein radius. We see no significant bias however and believe that the scatter is largely coming from the convergence fits.

(3) From the EAGLE Reference model we find that the mass density slope of galaxies inferred from lens modelling (t_{LENSED}) and

direct fitting (t_{NM}) generally agree well with the ratio, $t_{\text{NM}}/t_{\text{LENSED}}$, having a mean of 0.91 and standard deviation of 0.17 (Fig. 9).

(4) The lens modelling yields a mean density slope of $t = 2.26$ (an SIE has $t = 2$). Direct fitting, though, shows that this slope has a typical rms of 0.15 with that from lensing, setting a limit to the level to which the density slope can be determined (at least in these simulations). The average total density slope is higher than for SL2S, $t = 2.16$ or SLACS, $t = 2.08$ (Fig. 12). This slight difference within rms can be due to the feedback mechanisms and subgrid physics adopted in simulations, and also due to systematics.

(5) The complex ellipticity of EAGLE and SLACS lenses shows that three quarters of the modelled EAGLE lenses agree quite well with the distribution of SLACS lenses which is shown by the shaded region (Fig. 13). Ten out of twelve of the more elliptical simulated lenses have stellar mass $< 10^{11}$ $M_\odot$. Modelled complex-ellipticities for SL2S lenses are much more degenerate and EAGLE results are well within the SL2S lens domains. This larger ellipticity of SL2S lenses might also be due to the group environment in which the lenses resides. Although a degeneracy exists between q and ϕ but for massive ETGs in EAGLE we find broad agreement with SLACS and SL2S lenses.

In this work we have presented a pipeline to create and model simulated realistic mock strong lenses and a pilot comparison between EAGLE lenses and SLACS and SL2S lenses. Even though previous works (e.g. Xu et al. 2012) have simulated lenses and tested lensing degeneracies, we have extended those studies by incorporating the aspects of lens modelling and by comparing the inputs to quantify systematic effects in lens modelling. Moreover this work also aims at a full automation of simulated lens creation, modelling, and comparison with observation which will be needed when future surveys start discovering 1000s of strong lenses. In the future, we will use the SEAGLE pipeline to analyse various galaxy formation scenarios of EAGLE, and compare them to observations in order to disentangle various aspects of galaxy formation mechanisms.
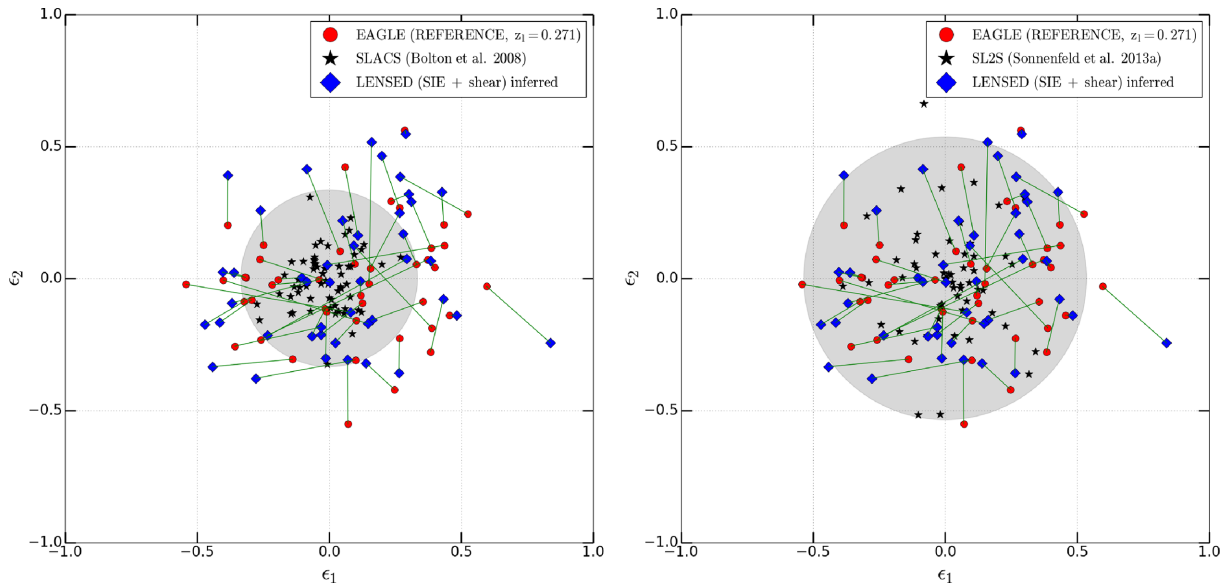
Figure 13. Comparison of the axial ratio and position angle of the EAGLE lenses (total modelled sample) with SLACS (left-hand panel) and SL2S (right-hand panel). The shaded region shows the maximum spread of the SLACS and SL2S lenses in left-hand and right-hand panels, respectively. 12 out of 45 EAGLE lenses fall completely outside of the SLACS range. Whereas only 2 out of 45 EAGLE lenses are beyond SL2S range. This indicates that the modelled parameters for SL2S are more degenerate than SLACS or might also intrinsically be having a larger spread in ellipticity due to their group environment. We have rejected one SL2S data point (SL2S J221326 − 000946) (located at the corner of the legend box in the right-hand panel plot) which we consider to be a critical failure in SL2S comparison plot (see Section 6.5).

REFERENCES

Auger M. W., Treu T., Bolton A. S., Gavazzi R., Koopmans L. V. E., Marshall P. J., Bundy K., Moustakas L. A., 2009, ApJ, 705, 1099
Auger M. W., Treu T., Gavazzi R., Bolton A. S., Koopmans L. V. E., Marshall P. J., 2010a, ApJ, 721, L163
Auger M. W., Treu T., Bolton A. S., Gavazzi R., Koopmans L. V. E., Marshall P. J., Moustakas L. A., Burles S., 2010b, ApJ, 724, 511
Balogh M. L., Morris S. L., 2000, MNRAS, 318, 703
Bandara K., Crampton D., Peng C., Simard L., 2013, ApJ, 777, 1
Bardeen J. M., Bond J. R., Kaiser N., Szalay A. S., 1986, ApJ, 304, 15
Barnes J. E., Hernquist L., 1992, ARA&A, 30, 705
Barnes J. E., Hut P., 1989, ApJS, 70, 389
Bellagamba F., Tessore N., Metcalf R. B., 2017, MNRAS, 464, 4823
Bender R., Burstein D., Faber S. M., 1992, ApJ, 399, 462
Bender R., Burstein D., Faber S. M., 1993, ApJ, 411, 153
Blumenthal G. R., Faber S. M., Primack J. R., Rees M. J., 1984, Nature, 311, 517
Bolton A. S., Burles S., Koopmans L. V. E., Treu T., Moustakas L. A., 2006, ApJ, 638, 703
Bolton A. S., Burles S., Koopmans L. V. E., Treu T., Gavazzi R., Moustakas L. A., Wayth R., Schlegel D. J., 2008a, ApJ, 682, 964
Bolton A. S., Burles S., Koopmans L. V. E., Treu T., Gavazzi R., Moustakas L. A., Wayth R., Schlegel D. J., 2008b, ApJ, 682, 964
Brownstein J. R. et al., 2012, ApJ, 744, 41
Cabanac R. A. et al., 2007, A&A, 461, 813
Chabrier G., 2003, PASP, 115, 763
Crain R. A. et al., 2009, MNRAS, 399, 1773
Crain R. A. et al., 2015, MNRAS, 450, 1937
Dobler G., Keeton C. R., Bolton A. S., Burles S., 2008, ApJ, 685, 57
Dolag K., Borgani S., Murante G., Springel V., 2009, MNRAS, 399, 497
Dutton A. A., Treu T., 2014, MNRAS, 438, 3594
Eggen O. J., 1965, ARA&A, 3, 235

Faber S. M., Jackson R. E., 1976, ApJ, 204, 668
Fall S. M., 1983, in Athanassoula E., ed., Proc. IAU Symp. 100, Internal Kinematics and Dynamics of Galaxies. Reidel, Dordrecht, p. 391
Feroz F., Hobson M. P., 2008, MNRAS, 384, 449
Feroz F., Hobson M. P., Bridges M., 2009, MNRAS, 398, 1601
Feroz F., Hobson M. P., Cameron E., Pettitt A. N., 2013, preprint (arXiv: 1306.2144)
Frenk C. S., White S. D. M., Efstathiou G., Davis M., 1985, Nature, 317, 595
Frenk C. S. et al., 1999, ApJ, 525, 554
Fukugita M., Peebles P. J. E., 2006, ApJ, 639, 590
Furlong M. et al., 2015, MNRAS, 450, 4486
Furlong M. et al., 2017, MNRAS, 465, 722
Gao L., White S. D. M., Jenkins A., Stoehr F., Springel V., 2004, MNRAS, 355, 819
Gavazzi R., Treu T., Rhodes J. D., Koopmans L. V. E., Bolton A. S., Burles S., Massey R. J., Moustakas L. A., 2007, ApJ, 667, 176
Gavazzi R., Treu T., Koopmans L. V. E., Bolton A. S., Moustakas L. A., Burles S., Marshall P. J., 2008, ApJ, 677, 1046
Gavazzi R., Treu T., Marshall P. J., Brault F., Ruff A., 2012, ApJ, 761, 170
Gavazzi R., Marshall P. J., Treu T., Sonnenfeld A., 2014, ApJ, 785, 144
Gunn J. E., Gott J. R., III, 1972, ApJ, 176, 1
Kazantzidis S., Zentner A. R., Kravtsov A. V., 2006, ApJ, 641, 647
Koopmans L. V. E., Treu T., Bolton A. S., Burles S., Moustakas L. A., 2006, ApJ, 649, 599
Koopmans L. V. E. et al., 2009, ApJ, 703, L51
Kormann R., Schneider P., Bartelmann M., 1994, A&A, 284, 285
Laureijs R. et al., 2011, preprint (arXiv:1110.3193)
Le Brun A. M. C., McCarthy I. G., Schaye J., Ponman T. J., 2014, MNRAS, 441, 1270
Lemson G., Springel V., 2006, in Gabriel C., Arviset C., Ponz D., Enrique S., eds, ASP Conf. Ser. Vol. 351, Astronomical Data Analysis Software and Systems XV. Astron. Soc. Pac., San Francisco, p. 212
Loeb A., Peebles P. J. E., 2003, ApJ, 589, 29
Marshall P. J. et al., 2007, ApJ, 671, 1196
McAlpine S. et al., 2016, Astron. Comput., 15, 72

Metcalf R. B., Petkova M., 2014, MNRAS, 445, 1942

Moore B., Ghigna S., Governato F., Lake G., Quinn T., Stadel J., 1998, in Zaritsky D., ed., ASP Conf. Ser. Vol. 136, Galactic Halos. Astron. Soc. Pac., San Francisco, p. 426

Navarro J. F., Frenk C. S., White S. D. M., 1996, ApJ, 462, 563

Nelder J. A., Mead R., 1965, Comput. J., 7, 308

Newton E. R., Marshall P. J., Treu T., Auger M. W., Gavazzi R., Bolton A. S., Koopmans L. V. E., Moustakas L. A., 2011, ApJ, 734, 104

Ostriker J. P., Hausman M. A., 1977, ApJ, 217, L125

Peebles P. J. E., 1982, ApJ, 263, L1

Petkova M., Metcalf R. B., Giocoli C., 2014, MNRAS, 445, 1954

Planck Collaboration XVI, 2014, A&A, 571, A16

Press W. H., Schechter P., 1974, ApJ, 187, 425

Remus R.-S., Dolag K., Naab T., Burkert A., Hirschmann M., Hoffmann T. L., Johansson P. H., 2017, MNRAS, 464, 3742

Ruff A. J., Gavazzi R., Marshall P. J., Treu T., Auger M. W., Brault F., 2011, ApJ, 727, 96

Rusin D., Kochanek C. S., 2005, ApJ, 623, 666

Rusin D. et al., 2003a, ApJ, 587, 143

Rusin D., Kochanek C. S., Keeton C. R., 2003b, ApJ, 595, 29

Sand D. J., Treu T., Smith G. P., Ellis R. S., 2004, ApJ, 604, 88

Schaller M. et al., 2015a, MNRAS, 451, 1247

Schaller M., Dalla Vecchia C., Schaye J., Bower R. G., Theuns T., Crain R. A., Furlong M., McCarthy I. G., 2015b, MNRAS, 454, 2277

Schaye J. et al., 2010, MNRAS, 402, 1536

Schaye J. et al., 2015, MNRAS, 446, 521

Schweizer F., 1982, ApJ, 252, 455

Searle L., Zinn R., 1978, ApJ, 225, 357

Segers M. C., Schaye J., Bower R. G., Crain R. A., Schaller M., Theuns T., 2016, MNRAS, 461, L102

Sersic J. L., 1968, Atlas de galaxias australes

Shu Y. et al., 2015, ApJ, 803, 71

Shu Y. et al., 2017, ApJ, 851, 48

Skilling J., 2006, Bayesian Anal., 1, 833

Sonnenfeld A., Gavazzi R., Suyu S. H., Treu T., Marshall P. J., 2013a, ApJ, 777, 97

Sonnenfeld A., Treu T., Gavazzi R., Suyu S. H., Marshall P. J., Auger M. W., Nipoti C., 2013b, ApJ, 777, 98

Sonnenfeld A., Treu T., Marshall P. J., Suyu S. H., Gavazzi R., Auger M. W., Nipoti C., 2015, ApJ, 800, 94

Springel V., 2010, MNRAS, 401, 791

Springel V., Yoshida N., White S. D. M., 2001, New Astron., 6, 79

Springel V., Di Matteo T., Hernquist L., 2005a, MNRAS, 361, 776

Springel V. et al., 2005b, Nature, 435, 629

Springel V., Frenk C. S., White S. D. M., 2006, Nature, 440, 1137

Tagore A. S., Barnes D. J., Jackson N., Kay S. T., Schaller M., Schaye J., Theuns T., 2018, MNRAS, 474, 3403

Tessore N., Metcalf R. B., 2015, A&A, 580, A79

Tessore N., Bellagamba F., Metcalf R. B., 2016, MNRAS, 463, 3115

Toomre A., Toomre J., 1972, ApJ, 178, 623

Tortora C., La Barbera F., Napolitano N. R., Romanowsky A. J., Ferreras I., de Carvalho R. R., 2014, MNRAS, 445, 115

Trayford J. W. et al., 2015, MNRAS, 452, 2879

Trayford J. W. et al., 2017, MNRAS, 470, 771

Treu T., Koopmans L. V. E., 2004, ApJ, 611, 739

Treu T., Koopmans L. V., Bolton A. S., Burles S., Moustakas L. A., 2006, ApJ, 640, 662

Treu T., Gavazzi R., Gorecki A., Marshall P. J., Koopmans L. V. E., Bolton A. S., Moustakas L. A., Burles S., 2009, ApJ, 690, 670

Tully R. B., Somerville R. S., Trentham N., Verheijen M. A. W., 2002, ApJ, 569, 573

Vogelsberger M., Sijacki D., Kereš D., Springel V., Hernquist L., 2012, MNRAS, 425, 3024

Vogelsberger M. et al., 2014, MNRAS, 444, 1518

White S. D. M., Rees M. J., 1978, MNRAS, 183, 341

Xu D. D., Mao S., Cooper A. P., Gao L., Frenk C. S., Angulo R. E., Helly J., 2012, MNRAS, 421, 2553
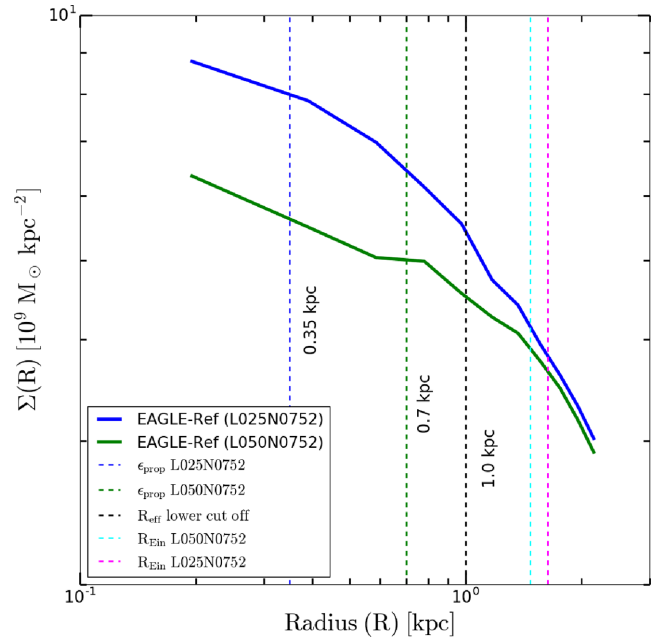
Figure A1. Comparison of the surface mass density profile of two example ETGs extracted from the EAGLE-Reference runs L050N0752 and L025N0752 having similar stellar masses ($M_\star \sim 10^{10.6}$ $M_\odot$). The effect of the smoothing kernel can be visualized when the slope flattens at their respective softening lengths. The Einstein radii 1.63 and 1.47 kpc are also shown for the galaxy in L025N0752 (magenta dashed line) and L050N0752 (cyan dashed line) simulation, respectively.

Xu D., Springel V., Sluse D., Schneider P., Sonnenfeld A., Nelson D., Vogelsberger M., Hernquist L., 2017, MNRAS, 469, 1824

APPENDIX A: CORES IN SIMULATIONS AND MASKING

Here we show how the spatial resolution affects the inner (<1 kpc) region of EAGLE galaxies. We used two simulation boxes of EAGLE-Reference run, i.e. L050N0752 and L025N0752 (the latter with higher resolution). In Fig. A1 we plot the surface mass density versus the radius for an example galaxy (after projection and lens creation). We can see that the slopes flatten at their respective softening lengths (represented by ϵ_{prop}, as in Table 1). The radius where the two density profiles start to converge is well inside the Einstein radii of these galaxies.

However, the effect of smoothing in the central region does not bias the strong lensing analysis, since we mask out the inner 7×7 pixels, which correspond to 1.4×1.4 kpc. Masking is a standard practice in observational analysis, too, where strong lenses are analysed after masking out the lensing galaxy. In order to not bias the results from simulation and to make an unbiased comparison with direct fitting results we perform this masking operation in our simulated galaxies (see Section 3). This aspect is very important as the cores can skew the density slopes obtained directly from simulations, if the mask is not used.

APPENDIX B: EFFECT OF SOURCE SIZES AND PRIOR TYPES

We have used a subsample of our simulated lenses to access the impact of source sizes and different prior settings. There lensing galaxies having $M_\star > 10^{11}$ $M_\odot$ projected along three axes have

Table B1. Comparison of the modelled density slopes and shear having different prior settings in LENSED and using different source sizes. We note that the differences are minor and much smaller than the spread between systems or their typical errors (t_L is ± 0.05 and $\gamma_{1,2}$ is ± 0.001).

	EPL-Gaussian			EPL-uniform		
Prior on t_L	$\mu = 1.1, \sigma = 0.1$			$0 - 2$		
Prior on $\gamma_1 \gamma_2$	$\mu = 0.0, \sigma = 0.01$			$-0.1 - 0.1$		
Source	t_L	γ_1	γ_2	t_L	γ_1	γ_2
Sérsic,[a] $R_{\mathrm{eff}} = 0.2$	1.06	-0.040	0.021	1.05	-0.041	0.021
Sérsic,[a] $R_{\mathrm{eff}} = 0.3$	1.08	-0.038	0.020	1.05	-0.039	0.021
Sérsic,[a] $R_{\mathrm{eff}} = 0.4$	1.06	-0.036	0.020	1.04	-0.040	0.021

[a]All other source parameters have been kept same as Table 3.

been used. So lens-modelling results from a total of nine lenses have been presented here.

In Table B1 we summarize the effect of different source sizes and prior types on the mean results of modelled density mass slope (t_L)

and shear components (γ_1 and γ_2). We used two different families of prior settings: Gaussian and uniform. The values of the priors (the mean μ and standard deviation σ for Gaussian priors and *minimum* and *maximum* of the range of values for uniform priors) are tabulated in Table B1. We find that there is no substantial effect of the priors on the final result. In this paper we used the Gaussian priors on t_L since the computational time is decreased by 30–40 per cent with respect to using uniform priors.

We also note that there is no significant improvement in the final results using more spatially extended sources. This is expected since with $R_{\mathrm{eff}} = 0.2$ arcsec (typical SLACS source size; see Newton et al. 2011) for an *HST*-ACS filter, the S/N is already sufficient to constrain lens parameters.

This paper has been typeset from a TeX/LaTeX file prepared by the author.